Irrgang, C., Saynisch, J., Thomas, M. (2017): Utilizing oceanic electromagnetic induction to constrain an ocean general circulation model: A data assimilation twin experiment. - *Journal of Advances in Modeling Earth Systems*, *9*, 3, pp. 1703—1720.

DOI: http://doi.org/10.1002/2017MS000951

AGU PUBLICATIONS

Journal of Advances in Modeling Earth Systems

RESEARCH ARTICLE

10.1002/2017MS000951

Key Points:
- The modeled ocean-induced magnetic field is improved up to 17% globally and up to 54% locally
- Recovery of ocean velocities is enhanced by up to 7% globally and over the whole water column
- False corrections are linked to deficient error covariance estimates and wind stress adjustments

Correspondence to:
C. Irrgang,
irrgang@gfz-potsdam.de

Citation:
Irrgang, C., J. Saynisch, and M. Thomas (2017), Utilizing oceanic electromagnetic induction to constrain an ocean general circulation model: A data assimilation twin experiment, *J. Adv. Model. Earth Syst.*, *9*, 1703–1720, doi:10.1002/2017MS000951.

Received 20 FEB 2017
Accepted 17 JUN 2017
Accepted article online 20 JUN 2017
Published online 17 JUL 2017

Utilizing oceanic electromagnetic induction to constrain an ocean general circulation model: A data assimilation twin experiment

Christopher Irrgang[1,2], Jan Saynisch[1], and Maik Thomas[1,2]

[1]Helmholtz Centre Potsdam, GFZ German Research Centre for Geosciences, Section 1.3: Earth System Modelling, Potsdam, Germany, [2]Institute of Meteorology, Freie Universität Berlin, Berlin, Germany

Abstract Satellite observations of the magnetic field induced by the general ocean circulation could provide new constraints on global oceanic water and heat transports. This opportunity is investigated in a model-based twin experiment by assimilating synthetic satellite observations of the ocean-induced magnetic field into a global ocean model. The general circulation of the world ocean is simulated over the period of 1 month. Idealized daily observations are generated from this simulation by calculating the ocean-induced magnetic field at 450 km altitude and disturbing these global fields with error estimates. Utilizing an ensemble Kalman filter, the observations are assimilated into the same ocean model with a different initial state and different atmospheric forcing. Compared to a reference simulation without data assimilation, the corrected ocean-induced magnetic field is improved throughout the whole simulation period and over large regions. The global RMS differences of the ocean-induced magnetic field are reduced by up to 17%. Local improvements show values up to 54%. RMS differences of the depth-integrated zonal and meridional ocean velocities are improved by up to 7% globally, and up to 50% locally. False corrections of the ocean model state are identified in the South Pacific Ocean and are linked to a deficient estimation of the ocean model error covariance matrices. Most Kalman filter induced changes in the ocean velocities extend from the sea surface down to the deep ocean. Allowing the Kalman filter to correct the wind stress forcing of the ocean model is essential for a successful assimilation.

Plain Language Summary Numerical simulations of the general ocean circulation resemble reality only up to a limited degree. Therefore, numerical models are often combined with actual observations to improve the reliability of computational results. In this study, we investigate the usage of a novel set of observations, namely satellite measurements of ocean-induced magnetic signals.Seawater is a highly conductive medium. By moving through the magnetic core field of the Earth, ocean flow generates characteristic magnetic signals, which are emitted outside of the ocean into space. Satellite observations of these ocean-induced magnetic signals could be used as a measure of oceanic transports of water, heat, and salinity.In this study, we investigate the benefits and challenges of using satellite observations of the ocean-induced magnetic field to correct a global ocean model. The results show that simulated large-scale ocean currents can be corrected with this technique, if high-quality satellite observations are provided and if the uncertainties of the ocean model can be estimated accurately.

1. Introduction

Electromagnetic induction in the ocean arises from interactions between the highly conducting salt water and the ambient geomagnetic field. *Sanford* [1971] showed that these motionally induced magnetic signals are to first order proportional to the conductivity-weighted and depth-integrated ocean velocities. Measurements (e.g., by satellites) of the induced magnetic signals could serve as additional observations of the general ocean circulation and provide a new opportunity to constrain oceanic water and heat transports in ocean models.

Based on the early pioneering work of *Larsen* [1968], *Sanford* [1971], *Cox* [1981], *Chave* [1983], and *Chave and Luther* [1990], several studies were conducted during the last two decades that aimed to characterize both tide and circulation-induced magnetic fields by using ocean models. Among others, electromagnetic

induction due to the general ocean circulation was investigated by *Stephenson and Bryan* [1992], *Flosadóttir et al.* [1997], *Tyler et al.* [1997], *Vivier et al.* [2004], *Manoj et al.* [2006], and *Irrgang et al.* [2016a]. Since tidal-induced magnetic signals are now readily extracted from satellite measurements [*Tyler et al.*, 2003; *Sabaka et al.*, 2016], practical applications of these signals were investigated, e.g., probing the conductivity of the lithosphere [*Schnepf et al.*, 2015; *Grayver et al.*, 2016] and detecting long-term changes in the sea water conductivity due to climate variability [*Saynisch et al.*, 2016]. The influence of uncertainties and erroneous input data on the modeling of electromagnetic induction in the ocean was recently analyzed by *Irrgang et al.* [2016b].

In this study, we explore a new application of oceanic electromagnetic induction, i.e., the correction of an ocean general circulation model by assimilating satellite observations of the ocean-induced magnetic field. This is especially rewarding for ocean modeling, since potential magnetic field satellite observations provide integrated information about ocean flow from the sea surface down to the bottom of the ocean.

ESA's Swarm mission measures the magnetic field of the Earth with unprecedented precision. The detection of signals from the general ocean circulation was defined in the Swarm research objectives [*Friis-Christensen et al.*, 2006]. However, in contrast to the easier detectable tidal magnetic field [*Sabaka et al.*, 2016], ocean circulation induced magnetic signals have not yet been extracted from satellite observations (a review was presented by *Kuvshinov* [2008]). Additionally, it is unknown, whether such satellite observations depict suitable constraints for ocean models, since small-scale features of the smoothed ocean-induced magnetic field are not visible at satellite altitude [*Manoj et al.*, 2006].

A model-based twin experiment is conducted in this study to investigate the potential of assimilating ocean-induced magnetic field satellite observations into an ocean general circulation model. For this, it is assumed that a processed and idealized data product with motional induction satellite observations exists. The ocean model together with an electromagnetic induction model is utilized to generate a set of synthetic, i.e., artificial, and idealized observations in the form of global fields. The observations are disturbed with Gaussian white noise. The data assimilation is performed with an ensemble-based Kalman filter. The calculation of the ocean model error covariance matrices bases on the findings of *Irrgang et al.* [2016b], whereas the observation error covariance matrix is estimated from the observation noise level based on the nominal Swarm precision of 0.1 nT [*Friis-Christensen et al.*, 2006; *Olsen et al.*, 2006]. The impact of the assimilation on the model trajectories is quantified with respect to an unconstrained forward simulation. This experiment setup allows analyzing and quantifying the Kalman filter impact on the individual components of the ocean model state in a consistent way. Additionally, problems arising due to the data assimilation are identified and discussed.

This paper is structured as follows. In section 2, the numerical models are described. The twin experiment setup together with the utilized data assimilation scheme and the generation of the synthetic observations are illustrated. In section 3, the performance of the data assimilation and the impact on the model results are presented and discussed. In section 4, a summary and conclusions are given.

2. Methodology

2.1. Model Setup

2.1.1. Global Ocean Model

The general circulation of the world ocean is simulated with the Ocean Model for Circulation and Tides (OMCT) [*Thomas et al.*, 2001]. OMCT is a baroclinic free-surface ocean model and bases on nonlinear balance equations for momentum, the continuity equation, and conservation equations for salt and heat. The hydrostatic and the Boussinesq approximations are applied. Artificial mass change caused by the Boussinesq approximation is corrected as proposed by *Greatbatch* [1994]. According to K-theory, a turbulence closure scheme is applied by specifying horizontal eddy diffusivity and vertical eddy viscosity constants, respectively. The longitudinal and latitudinal resolution is 1.875°. OMCT is a z-model and the vertical is resolved by 13 layers. A time step of 30 min is used. OMCT is forced with wind stress, surface pressure, heat flux, precipitation, and evaporation. The forcing data are derived from 6 hourly ERA-Interim reanalysis products provided by the European Centre for Medium-Range Weather Forecasts (ECMWF) [*Dee et al.*, 2011]. Ocean tides are not simulated with the used configuration of the model.

In recent studies, OMCT has been used for various purposes [e.g., *Dobslaw and Thomas*, 2007; *Dobslaw et al.*, 2013; *Saynisch et al.*, 2014; *Irrgang et al.*, 2016a] and it realistically resolves the main features of the general

ocean circulation. Additionally, OMCT is suitable for simulating short timescales. The model has been operatively used to simulate submonthly ocean bottom pressure anomalies for dealiasing gravity observations from the GRACE (Gravity Recovery And Climate Experiment) satellites [*Dobslaw et al*., 2013]. The effect of small-scale features in the ocean circulation on the ocean-induced magnetic field [e.g., *Lilley et al*., 1993] is not reproduced by the current version of OMCT. However, since the aim of this study is the assimilation of synthetic magnetic field observations at satellite altitude, the resolution of the used models is sufficiently large. Any small-scale features that are present in the ocean-induced magnetic field near the sea surface are blurred with increasing height due to the smoothing effect by the upwardly continuation of the induced signal [*Vennerstrom et al*., 2005; *Manoj et al*., 2006].

2.1.2. Electromagnetic Induction Model

The electromagnetic induction model is used to derive synthetic observations of the ocean-induced magnetic field at satellite altitude (see section 2.2.3). In the data assimilation scheme, it is applied as a global observation operator of the general ocean circulation (see section 2.2.2). The model calculates the radial component of the primary ocean-induced poloidal magnetic field, which is generated by the large-scale horizontal ocean circulation and emitted outside of the ocean. The primary toroidal ocean-induced magnetic field component [*Chave*, 1983] and secondary poloidal magnetic signals near continental borders [*Szuts*, 2010; *Dostal et al*., 2012] are not considered in this model.

Based on a 2-D induction equation as described by *Tyler et al*. [1997] and *Vivier et al*. [2004], the electromagnetic induction source is calculated in a thin-shell approximation of the ocean basin. This thin shell only contains conductivity-weighted and depth-integrated horizontal ocean velocities and induced electric currents. Vertical ocean flow is neglected in this approach. The thin shell is supplemented by an underlying layer of conductive ocean sediments, whereas the atmosphere and upper mantle are treated as insulators [*Parkinson and Hutton*, 1989; *Vivier et al*., 2004]. The layer of conductive ocean sediments is derived by applying a heuristic method described by *Everett et al*. [2003] to the sediment thickness maps of *Laske and Masters* [1997].

In the thin shell, Ampere's law and Ohm's law are simplified and induced horizontal electric currents can be expressed by an electric stream function ψ_e [*Vivier et al*., 2004], which is calculated from the scalar model equation

$$\nabla \cdot \left(\Sigma^{-1}\nabla\psi_e\right) = \nabla \cdot \left(\Sigma^{-1} F_r \int_h \sigma \boldsymbol{u}_H dr\right). \tag{1}$$

Here h is the variable thickness of the thin shell according to the bathymetry, Σ is the depth-integrated conductivity of the water column and underlying sediments, σ is the conductivity at a given point (ϕ, ϑ, z), F_r is the radial part of the ambient geomagnetic field, and $\boldsymbol{u}_H$ is the horizontal ocean flow velocity. F_r is derived from the POMME-6 Magnetic Model of the Earth [*Maus et al*., 2010] and $\boldsymbol{u}_H$ is prognostically calculated with OMCT. The ocean-induced magnetic field $\boldsymbol{b}$ is expressed by the gradient of a potential field P as

$$\boldsymbol{b} = -\nabla P. \tag{2}$$

Given the nondivergence of the ocean-induced magnetic field, $\nabla \cdot \boldsymbol{b} = 0$, P can be derived from ψ_e through a boundary value problem, i.e.,

$$\nabla^2 P(\phi, \vartheta, r) = 0, \tag{3}$$

$$P(\phi, \vartheta, \infty) = 0, \tag{4}$$

$$P(\phi, \vartheta, a+\zeta) = -\frac{1}{2}\mu_0 \psi_e(\phi, \vartheta), \tag{5}$$

where a is the Earth's radius and ζ is the sea surface height. The solution for P is given by a spherical harmonics expansion according to

$$P(\phi, \vartheta, r) = -\sum_{j=0}^{\infty} \sum_{m=-j}^{j} \frac{1}{2}\mu_0 \psi_{jm} \left(\frac{a}{r}\right)^{j+1} Y_{jm}(\phi, \vartheta). \tag{6}$$

Here ϕ and ϑ are longitudinal and colatitudinal coordinates on the sphere, μ_0 is the permeability of free space, a is the Earth's radius, r is the height above sea level, ψ_{jm} and $Y_{jm}(\phi, \vartheta)$ are the spherical harmonic coefficients and functions, respectively. The indices j and m are degree and order of the spherical

harmonics. The global radial component b_r of the ocean-induced magnetic field at satellite altitude is derived from the upwardly continuation of P to satellite altitude by

$$b_r(\phi,\vartheta,r)=\frac{\partial}{\partial r}P(\phi,\vartheta,r), \tag{7}$$

$$=\sum_{j=0}^{j_{max}}\sum_{m=-j}^{j}\frac{1}{2}\frac{\mu_0}{r}\psi_{jm}\left(\frac{a}{r}\right)^{j+1}(j+1)Y_{jm}(\phi,\vartheta). \tag{8}$$

As described in *Irrgang et al*. [2016a], the maximum degree j_{max} of the spherical harmonics expansion is limited to 47 in order to prevent aliasing artefacts during the grid transformations.

2.2. Data Assimilation

2.2.1. Kalman Filter

Data assimilation aims to combine a numerically calculated state forecast x^f of a geophysical system with observational data y. Kalman filters [*Kalman*, 1960] form one class of data assimilation techniques that sequentially assimilate observations into a model at the time they become available. At a time t where observations y_t are present, an analyzed state x_t^a is calculated by

$$x_t^a=x_t^f+K_t\left(y_t-H\left[x_t^f\right]\right). \tag{9}$$

H is the observation operator that projects the estimated state x_t^f into the observation space of y_t. Here H is the electromagnetic induction model that calculates the ocean-induced magnetic field for the state x_t^f at satellite altitude (see section 2.2.3). The matrix K_t is the Kalman gain at time t that depends on the error covariance matrices, i.e., uncertainty information, of the ocean model (P_t) and of the observations (R_t). Accordingly, a small (large) observation residual $y_t-H[x_t^f]$ results in a small (large) update of the model state x_t^f, which is weighted by the combined uncertainty information. Subsequently, the analyzed state x_t^a is propagated through time with the numerical model until the next observation is available (forecast phase).

In oceanography, data assimilation typically is a high-dimensional problem that involves state forecasts from nonlinear models with several thousand entries and cost-expensive inversions of the respective error covariance matrices. Therefore, ensemble Kalman filters [*Evensen*, 1994, 2003] and their error subspace variants (a description and comparison are presented in *Nerger et al*. [2005a]) are commonly used for efficiently assimilating observations with nonlinear and high-dimensional numerical models [e.g., *Pham et al*., 1998a; *Pham*, 2001; *Saynisch and Thomas*, 2012; *Saynisch et al*., 2014].

In this study, we use the localized error subspace transform Kalman filter (LESTKF) [*Nerger et al*., 2012a] from the parallel data assimilation framework (PDAF) [*Nerger et al*., 2005b]. The LESTKF is an error subspace ensemble Kalman filter and was constructed as a variant of the singular evolutive interpolated Kalman filter (SEIK) [*Pham et al*., 1998b] that performs minimum ensemble member transformations in the assimilation step. The exact formalism of equation (9) in the LESTKF is given by *Nerger et al*. [2012a].

The state forecast x^f contains six components that can be adjusted by the Kalman filter: 3-D fields of zonal (u) and meridional (v) ocean velocities, ocean temperature (T), ocean salinity (S); and 2-D fields of zonal (τ_x) and meridional (τ_y) wind stress forcing. During the forecast phase, the variables $u, v, S,$ and T are prognostically calculated with the OMCT, whereas τ_x and τ_y are read in from input data (see also section 2.1.1). Since *Irrgang et al*. [2016b] showed that errors in the wind stress forcing have a major impact on the ocean-induced magnetic field, the forcing fields τ_x and τ_y are also allowed to be adjusted in the assimilation step.

The initial state x_0^f and the uncertainty P_0 for the simulated month January are sampled by a 32-member ensemble, which is created by second-order exact sampling [*Pham*, 2001]. Larger ensemble sizes did not change the results of this study. The ensemble is generated such that the cross-ensemble variance represents the initial uncertainty provided by the error covariances in P_0. The ensemble members differ from each other by the initial OMCT state and by the wind stress of the atmospheric forcing. A detailed description of the ensemble generation and the calculation of the initial error covariance matrix P_0 is presented by *Irrgang et al*. [2016b] and is adopted for this study (see section 2.2.2). The observation error covariance matrix is chosen to be a time-invariant diagonal matrix, i.e., $R_t = R$. The variances on the diagonal of R are derived from the estimated error in the synthetic satellite observations (see section 2.2.3). All ensemble

members are propagated through time independently with the nonlinear ocean model until a new observation is available. After this forecast phase, the assimilation step (equation (9)) is performed on the cross-ensemble mean $\overline{x_t^f}$.

Localized Kalman filters as LESTKF are based on the assumption that only observations in close proximity to the currently analyzed grid point, or region, have an influence on the assimilation update [e.g., *Evensen*, 2003]. Therefore, both the mean state forecast $\overline{x_t^f}$ and the observation vector y_t are decomposed into local components before the assimilation step. The localization used in this version of LESTKF subdivides the ocean basin into disjoint vertical columns ($1\times1\ \times$ number of vertical grid points). The number of vertical columns is equal to the number of sea surface grid points. Each local state consists of one vertical ocean column and the corresponding values of the wind stresses τ_x and τ_y. The local state vectors are updated independently in the assimilation step according to equation (9). Although the ocean-induced magnetic field at satellite altitude is in principle nonlocal (due to the upwardly continuation, see section 2.1.2), the large-scale spatial distribution remains very similar to the magnetic field signals at the sea surface. On this basis, a quasi-local correspondence between the observed ocean-induced magnetic signal at a given location and the oceanic transport underneath is assumed. The observation y_t is localized for each local state by restricting the global observation field (see section 2.2.3) to a circular subset with a radius of eight grid points and its center located at the sea surface grid point of the local state. From a range of tested radii, the chosen radius of eight grid points provides the highest Kalman filter improvements. Consequently, the localized observations of two neighboring local states largely overlap. This ensures a smooth transition between the analyzed local states and the global analyzed state. After all local states have been updated by the Kalman filter, the global analyzed mean state $\overline{x_t^a}$ is reassembled from the local analyzed state vectors and the ensemble is updated. Subsequently, the next forecast phase starts. A detailed formulation of the localization scheme is presented by *Nerger et al.* [2012b].

2.2.2. Twin Experiment Setup

A model-based twin experiment is performed to investigate the performance of the data assimilation. The experiment setup is shown in Figure 1 and consists of three OMCT state trajectories with a length of 1 month. Snapshots, i.e., instantaneous values, of the ocean-induced magnetic field, ocean velocities, temperature, and salinity are stored once per day for all simulations.

The first simulation is called MAGTRUTH and simulates January 2001. MAGTRUTH represents the true state of the general ocean circulation in January. The synthetic satellite measurements of the ocean-induced magnetic field are generated from MAGTRUTH once per day (details follow in section 2.2.3). These observations are the only information, which are derived and utilized from the known true state of the general ocean circulation.

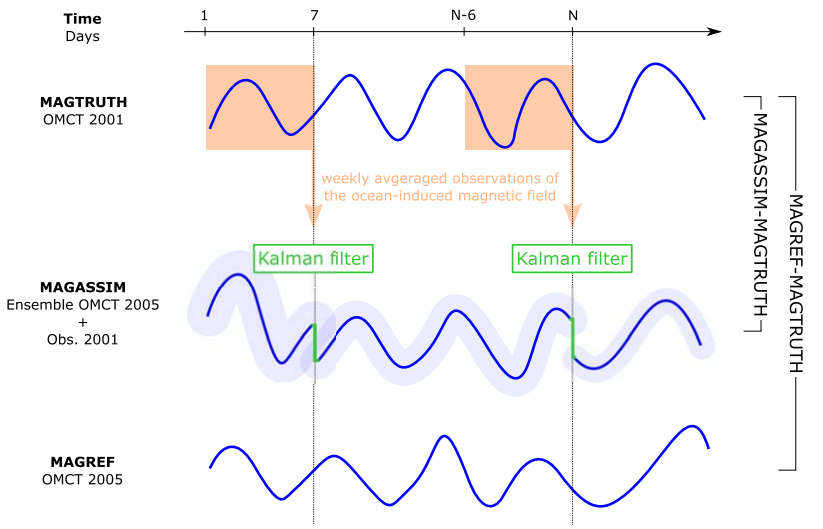

Figure 1. Sketch of the data assimilation twin experiment. The blue curves represent OMCT state trajectories. The synthetic observations are generated from MAGTRUTH and assimilated into MAGASSIM. MAGREF is a reference simulation without data assimilation. To evaluate the performance of the Kalman filter, the differences MAGASSIM minus MAGTRUTH and MAGREF minus MAGTRUTH are compared.

MAGREF represents a known unconstrained state of the general ocean circulation in January and serves as a reference simulation without data assimilation. The deviations in MAGREF from MAGTRUTH are generated by simulating the same time period of a different year, i.e., January 2005. Consequently, the deviations between MAGTRUTH and MAGREF result from different initial OMCT states and by the different responses of OMCT to the atmospheric forcing of the respective time periods (2001 versus 2005). The differences in the OMCT states between MAGREF and MAGTRUTH (MAGREF-MAGTRUTH) represent the error made by the ocean model to replicate the true prior state of the ocean.

To visualize the different ocean model states of MAGTRUTH and MAGREF, vector plots of both conductivity-weighted and depth-integrated ocean velocities and surface velocities are shown in Figure 2. The depicted monthly mean flows show distinct variations between the large-scale currents of both simulations. These are visible in all major depth-integrated ocean velocities, e.g., in western boundary currents, and in the Antarctic Circumpolar Current, but also in equatorial surface currents.

MAGASSIM is the simulation with data assimilation and aims to recover the true ocean state and ocean-induced magnetic field of MAGTRUTH. MAGASSIM has the same initial OMCT state and forcing as MAGREF. Starting from day 7, the synthetic satellite observations from MAGTRUTH are assimilated into MAGASSIM once per day. The differences in the OMCT states between MAGASSIM and MAGTRUTH (MAGASSIM-MAGTRUTH) represent the error between the corrected ocean model and the true prior state of the ocean (see also Figure 2).

As in a real-world data assimilation experiment with actual satellite observations of the ocean-induced magnetic field, it is assumed that the initial error covariance matrix P_0 of the ocean model in MAGASSIM is unknown and has to be estimated. For this, we utilize the common approach to estimate P_0 through the respective temporal variations of forward simulations during the considered time period [e.g., *Evensen*, 1994]. *Irrgang et al*. [2016b] calculated monthly error covariance matrices for each month of the year 2005.

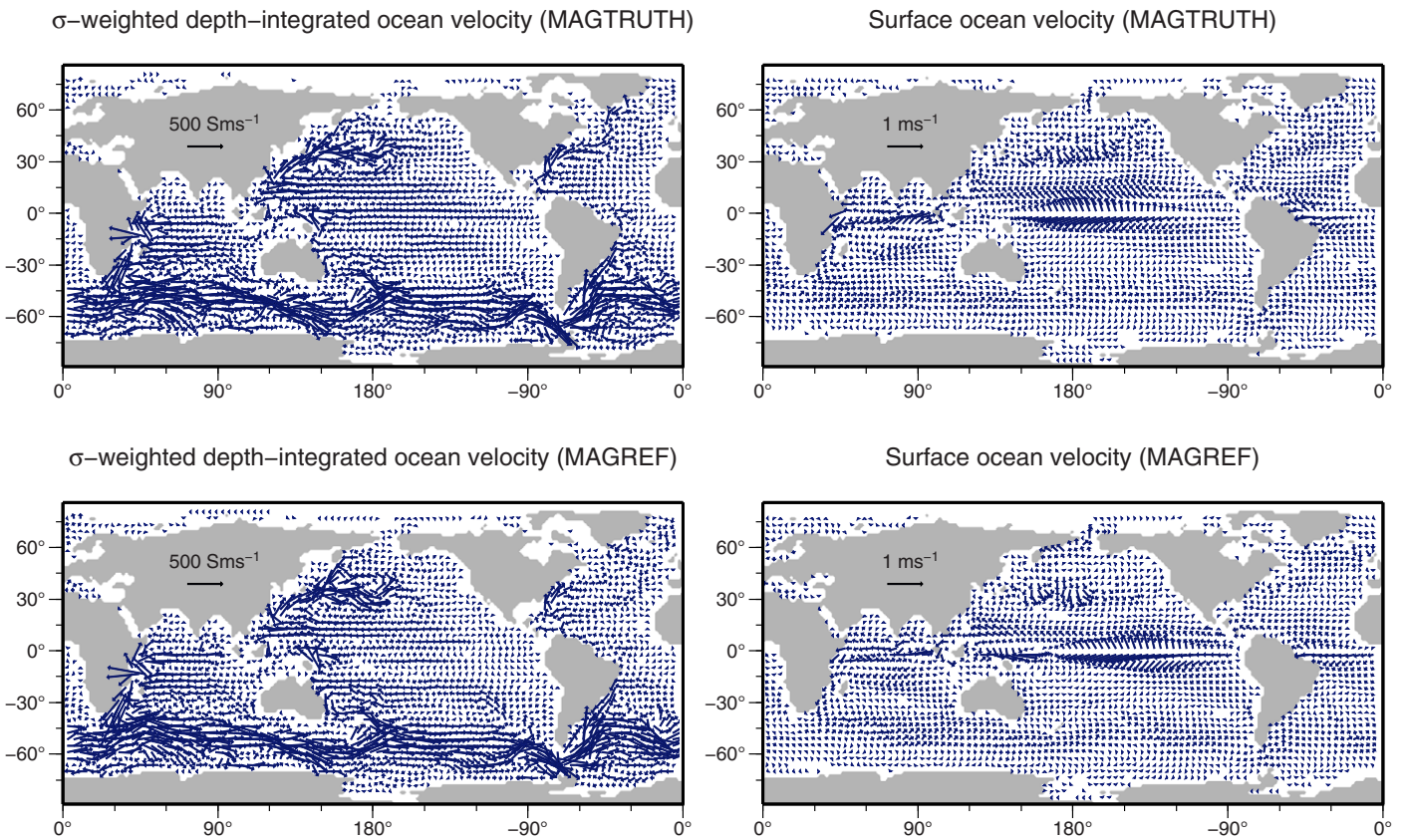

Figure 2. Ocean velocity vector plots of MAGTRUTH and of MAGREF at selected grid points. The left column shows conductivity-weighted and depth-integrated ocean velocities, the right column shows surface velocities of MAGTRUTH and MAGREF, respectively. Arrow lengths are mean values over the 1 month simulation time period.

Accordingly, for this data assimilation experiment the previously calculated error covariance matrix for the month January of 2005 is applied, which includes uncertainty estimates for the ocean model state (u, v, S, T), and for the atmospheric wind stress forcing (τ_x, τ_y). Consequently, this a priori estimation of P_0 is independent from the differences between the false and true ocean model states (MAGREF-MAGTRUTH), and solely the synthetic satellite observations from MAGTRUTH (see section 2.2.3) are utilized to provide information about the known true ocean state.

Due to the twin experiment setup, the deviations between MAGASSIM-MAGTRUTH and MAGREF-MAGTRUTH are a measure of the performance of the data assimilation. A decrease in MAGASSIM-MAGTRUTH compared to MAGREF-MAGTRUTH means a success of the data assimilation, i.e., the corrected ocean model recovers the known truth better than the reference, and vice versa. The choice of the years 2001 and 2005, i.e., the choice of true and false realizations of the general ocean circulation, is arbitrary and can also be made differently [e.g., *Saynisch et al*., 2015].

2.2.3. Synthetic Satellite Observations

The Swarm satellite trio measures the Earth's magnetic field with unprecedented precision and the detection of the general ocean circulation by its small induced magnetic signals was defined as one of the Swarm research objectives [*Friis-Christensen et al*., 2006]. Since *Tyler et al*. [2003] demonstrated the possibility to identify tidal (M2) magnetic signals in CHAMP satellite observations, several subsequent studies were performed to further characterize and utilize tide and circulation-induced magnetic signals [e.g., *Maus and Kuvshinov*, 2004; *Manoj et al*., 2006; *Schnepf et al*., 2015; *Grayver et al*., 2016; *Irrgang et al*., 2016a,b]. Recently, *Sabaka et al*. [2016] extracted the M2 and N2 ocean tide from 20.5 months of Swarm data. However, it remains a challenge to extract general circulation induced magnetic signals from satellite observations [see also *Kuvshinov*, 2008] and has so far not been achieved.

In this study, we assume that a data product with extracted and processed satellite observations of the general circulation induced magnetic field exists. The numerical models described in sections 2.1.1 and 2.1.2 are used to generate daily global fields that contain synthetic, i.e., artificial, and idealized satellite observations of ocean-induced magnetic signals (see Figure 3). The observations are calculated at a satellite altitude of 450 km above sea level. To overcome the lack of the temporal deviation in the EM-induction model (see section 2.1.2) and to smoothen the transition between two consecutive observations, each daily observation is a weekly average of its preceding seven days (see also the orange bins in Figure 1). Accordingly, the first observation at day 7 is generated from weekly averaged values over the days 1–7, the second observation at day 8 is generated from weekly averaged values over the days 2–8, and so on. From a range of tested setups of the observation operator, the usage of weekly averaged fields provided the best performance of the data assimilation (not shown). The uncertainty of the synthetic observations is modeled by adding uncorrelated Gaussian white noise with a standard deviation of 0.1 nT to each of the weekly averaged global fields. This matches with the nominal Swarm precision of 0.1 nT [*Friis-Christensen et al*., 2006;

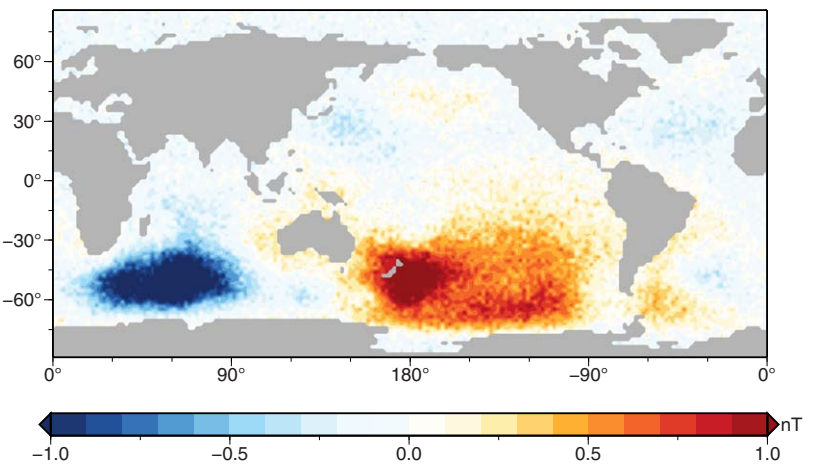

Figure 3. Synthetic observation field of the ocean-induced magnetic field. The map shows mean values over one week at satellite altitude (450 km) disturbed with uncorrelated Gaussian white noise (0.1 nT standard deviation).

Olsen et al., 2007]. The respective variance values of the Gaussian white noise are utilized as diagonal elements of the observation error covariance matrix *R*. As already stated in section 2.2.1, spatial error covariances, i.e., nondiagonal elements, in R are not considered in this study. As there is still only very limited knowledge about actual satellite observations of the ocean-induced magnetic field and its observational uncertainty, estimating the respective values in R would be speculative and does not provide additional conclusions in this twin experiment.

Due to several simplifications, the synthetic observations generated with this approach will naturally differ from actual satellite observations. The thin-sheet electromagnetic induction model assumes an insulating atmosphere and mantle (see section 2.1.2). Additionally, a high spatial and temporal resolution is assumed by generating daily and global observation fields with uniform errors. In our data assimilation twin experiment (section 2.2.2), the described synthetic observations are derived from MAGTRUTH and assimilated into MAGASSIM. Since MAGTRUTH is governed by the same ocean model and electromagnetic induction model and its simplifications, the realization of the real world is also restricted by these simplifications. Consequently, the twin experiment together with the synthetic observations builds a consistent data assimilation test environment. The influence of more complex properties of observations (e.g., nonuniform temporal resolution, spatial gaps, nonuniform uncertainty, etc.) can also be investigated in a twin experiment approach but are not part of this first assimilation study. Instead, we investigate the principle possibility of recovering a known ocean state by assimilating observations of the ocean-induced magnetic field into an ocean general circulation model.

3. Results and Discussion

3.1. Assimilation Impact on the Ocean-Induced Magnetic Field

A first measure of the assimilation performance is the global impact of the Kalman filter on the assimilated variable, i.e., the ocean-induced magnetic field. Since the synthetic satellite observations are generated from weekly averaged fields (see section 2.2.3 and Figure 1), we consistently measure the impact on the ocean model by calculating temporal RMS differences over the same weekly average bins for each assimilation step. The global RMS differences of the ocean-induced magnetic field of MAGREF-MAGTRUTH and MAGASSIM-MAGTRUTH over the 1 month simulation period are depicted in Figure 4. A perfect replication of MAGTRUTH would lead to a global RMS difference of zero. The values of the global RMS differences reside in the range of 0.05–0.08 nT. Both purple lines show a strong nonstatic and nonlinear behavior. This is due to the nonlinear ocean model and its response to the highly variable atmospheric forcing. Since also the respective errors of the models and input data evolve in time [see *Irrgang et al*., 2016b], the experiment setup builds a challenging test environment for the Kalman filter.

Throughout the whole simulation period, the global RMS differences between the corrected ocean-induced magnetic field and the known true values (thin purple line in Figure 4) stay below the RMS differences between the reference and the truth (thick purple line in Figure 4). In other words, the true motional induction is consistently better recovered (in the global sense) by the corrected model than by the reference without data assimilation. The improvement of the global RMS remains larger than 5% in almost all assimilation steps and reaches values up to 17% (see gray line in Figure 4). The temporal mean improvement of the global RMS over the whole simulation period amounts to 8%. Due to the twin experiment setup, the differences MAGREF-MAGTRUTH and MAGASSIM-MAGTRUTH must be attributed to the impact of the Kalman filter. Consequently,

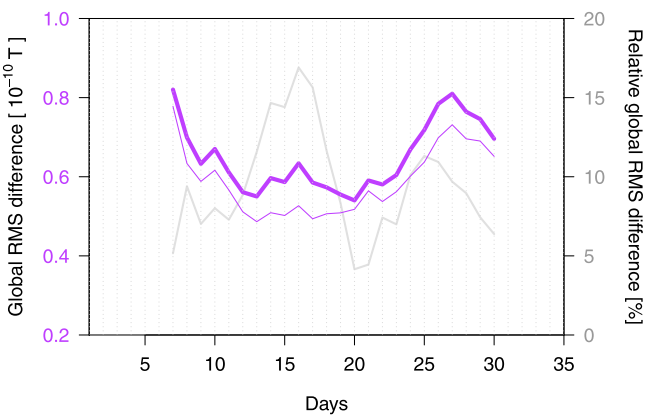

Figure 4. Global RMS differences of the MAGTRUTH ocean-induced magnetic field to MAGREF (thick purple line) and MAGASSIM (thin purple line). The relative difference between the two purple lines is depicted in gray.

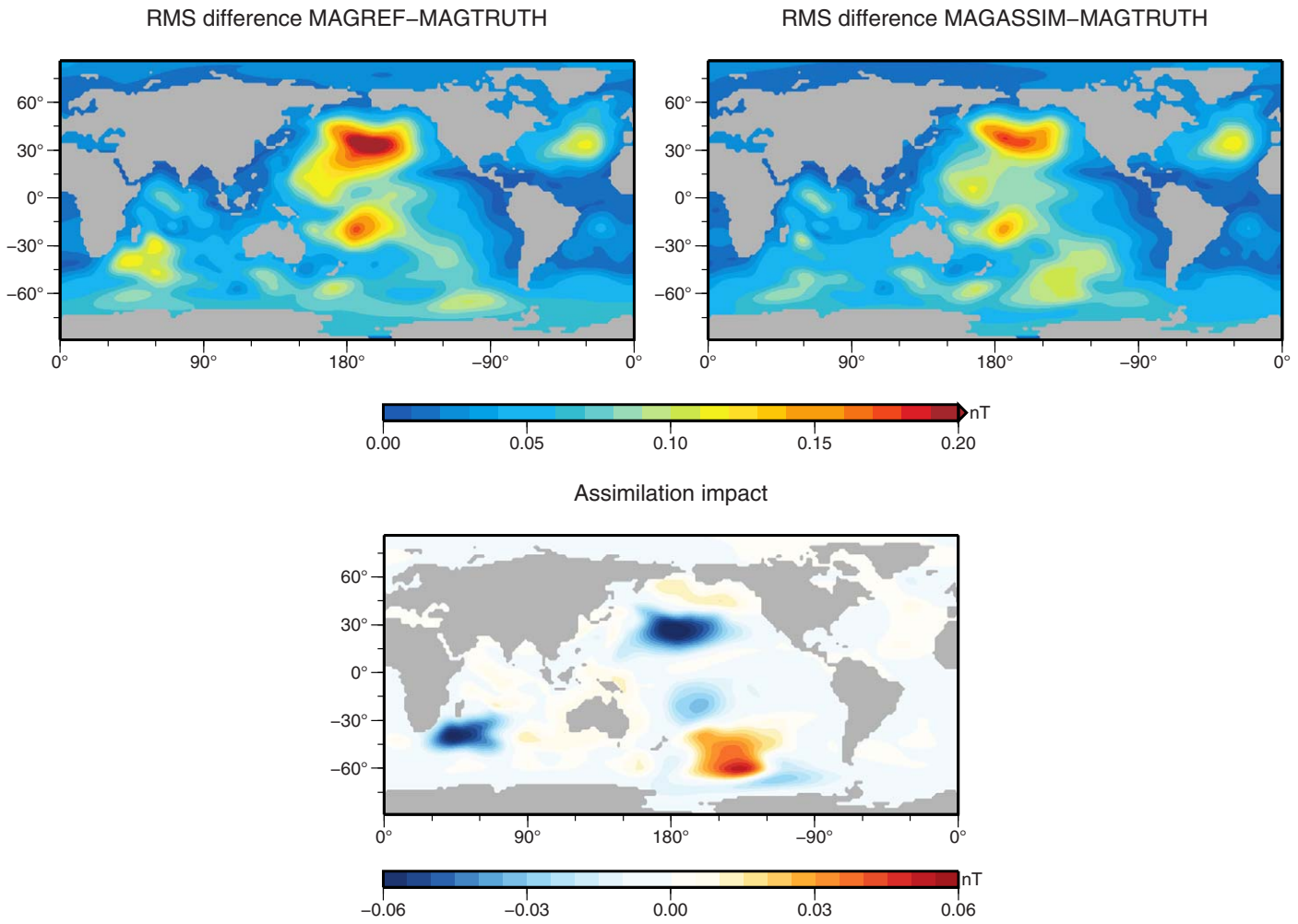

Figure 5. (top) RMS difference maps of the ocean-induced magnetic field of MAGREF-MAGTRUTH (left) and MAGASSIM-MAGTRUTH (right) over the whole simulation period. (bottom) Changes in the RMS difference due to the Kalman filtering (difference of the top maps). Blue areas indicate improvements, red areas indicate deteriorations.

it can be concluded that the assimilation of the synthetic observations has a positive effect on the models (in the global sense) and leads to an overall improvement of the modeled ocean-induced magnetic field.

To investigate the assimilation impact on the ocean-induced magnetic field in more detail, global misfit maps containing the temporal RMS differences over the whole simulation period are shown in Figure 5. The top left figure shows the misfit map between the reference and the truth with values of up to 0.22 nT. Note that this figure depicts the RMS error of the modeled ocean-induced magnetic field with respect to the known truth. Again, in the case of a perfect model replication of the true ocean-induced magnetic field, the misfit map would only show zero values. The highest RMS values with large-scale patterns are found in the North Pacific Ocean, east of Australia, east of South Africa, and in the North Atlantic Ocean. Generally, lower RMS values are present in the area of the Antarctic Circumpolar Current. As described in section 2.2.2, the misfit between MAGREF and MAGTRUTH is essentially determined by the different wind stress forcings in the respective simulation time periods. The spatial distribution of the misfit between MAGREF and MAGTRUTH shows similar patterns as the estimated uncertainty of the ocean-induced magnetic field due to the wind stress forcing [see *Irrgang et al.*, 2016b]. Since the wind stress forcing and its uncertainty are variable on various temporal scales [see also *Chaudhuri et al.*, 2013], the MAGREF-MAGTRUTH misfit will also show different values and patterns for different simulation time periods.

Figure 5 (top right) shows the RMS differences between MAGASSIM and MAGTRUTH. The maximum misfit is lower compared to MAGREF-MAGTRUTH with values up to 0.18 nT. The large-scale patterns in the North Atlantic Ocean and east of Australia are still present, but with generally lower values. The pattern east of

South Africa almost vanished. The misfit in the North Atlantic Ocean is only changed marginally and in the South Pacific Ocean a new pattern with values around 0.12 nT is visible.

The so-called assimilation impact (Figure 5, bottom) is the difference (MAGASSIM-MAGTRUTH)-(MAGREF-MAGTRUTH). It quantifies the changes due to the Kalman filter and shows values in the range of −0.07 and 0.05 nT. Here negative values indicate improvements due to the Kalman filter and positive values indicate deteriorations. From the assimilation impact, it can be seen that the misfit of the ocean-induced magnetic field is reduced in almost all regions. The Kalman filtering leads to improvements especially in the regions with the largest misfits (see Figure 5, upper left), i.e., in the North Pacific Ocean, east of Australia, and east of South Africa. The largest improvements correspond to a misfit reduction of up to 42% in the North Pacific Ocean and up to 54% in the region east of South Africa. In the South Pacific Ocean, the misfit between MAGASSIM and MAGTRUTH is larger than between MAGREF and MAGTRUTH, i.e., the Kalman filter introduced false corrections into the ocean-induced magnetic field in this region. Since the ocean-induced magnetic field is an integral quantity that is generated from several combined oceanic variables, there are many possible sources for the above described (positive and negative) impact of the Kalman filter. These sources are discussed in the following section.

3.2. Assimilation Impact on the Ocean Model State

The novel opportunity of assimilating ocean-induced magnetic field observations is to provide constraints to depth-integrated conductivity and velocities to the ocean model. In a first-order approximation, the ocean-induced magnetic field is proportional to the conductivity-weighted and depth-integrated ocean velocities [*Sanford*, 1971], which are calculated by the integral in equation (1). Therefore, we investigate the performance of the Kalman filter on these weighted depth-integrated velocities.

The global RMS differences of the conductivity-weighted and depth-integrated (hereafter called $\sigma-$depth$-$integrated) ocean velocities of MAGREF-MAGTRUTH and MAGASSIM-MAGTRUTH are depicted in Figure 6. The RMS differences reside in the range of 54 and 65 $\mathrm{S\,ms^{-1}}$ for the zonal (west-east) velocity and between 40 and 48 $\mathrm{S\,ms^{-1}}$ for the meridional (south-north) velocity. Similar to the ocean-induced magnetic field, both the zonal and meridional $\sigma-$depth$-$integrated velocities are corrected by the Kalman filter toward the truth (in the global sense) and show smaller RMS differences compared to the reference. The relative improvement amounts to up to 5% for the zonal component and up to 7% for the meridional component (see gray lines in Figure 6). The temporal mean improvements of the global RMS of the zonal and meridional components amount to 3 and 4%, respectively. Note that the $\sigma-$depth$-$integrated velocities are not corrected uniformly, i.e., the evolution of improvements varies between the two components. This results from the uncertainty estimation of the two components, i.e., the respective error covariances in P_t, that are used to weight the observation residual in the assimilation step (see equation (9)). This also underlines the importance of an accurate estimation of the error covariances between all state vector components in addition to the quality of the observations. Since the sediment conductance and the geomagnetic field are not corrected by the Kalman filter, the improvements in the ocean-induced magnetic field (see Figures 4 and 5) originate from the combined improvements in the $\sigma-$depth$-$integrated velocities (see equation (1)).

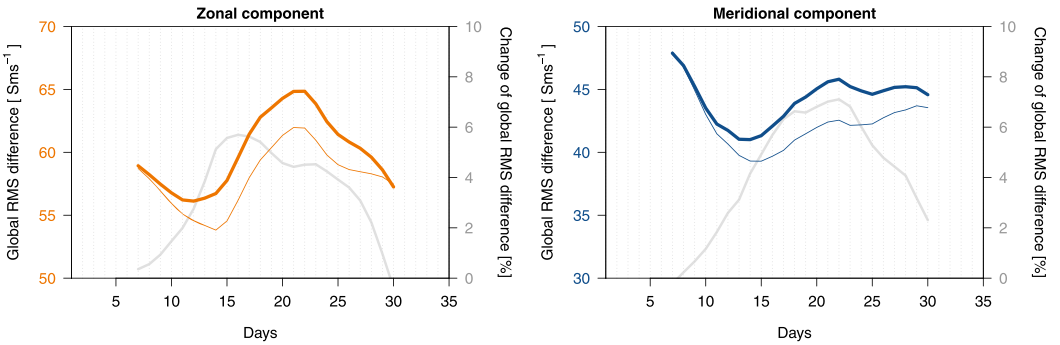

Figure 6. Global RMS differences MAGREF-MAGTRUTH (thick orange and thick blue lines) and MAGASSIM-MAGTRUTH (thin orange and thin blue lines) of the conductivity-weighted and depth-integrated ocean velocities. The relative difference for each pair of lines is depicted in gray.

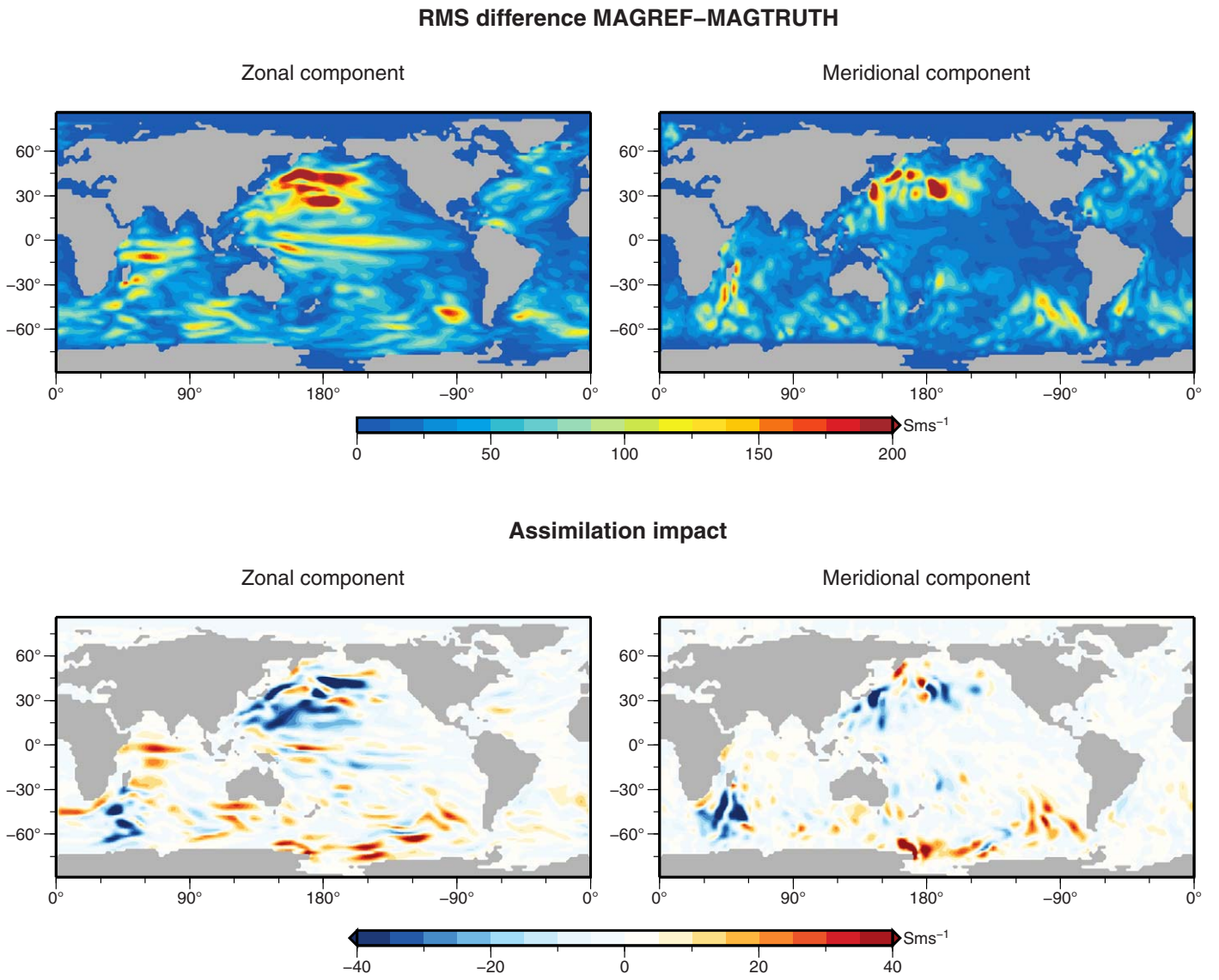

Figure 7. (top) RMS difference maps of the conductivity-weighted and depth-integrated ocean velocities of MAGREF-MAGTRUTH. (bottom) Changes in the RMS difference due to the Kalman filtering. Blue areas indicate improvements, red areas indicate deteriorations.

The MAGREF-MAGTRUTH misfit maps of the $\sigma-$depth$-$integrated velocities and the corresponding assimilation impacts are shown in Figure 7. Again, the assimilation impact quantifies the RMS impact of the Kalman filter on the zonal and meridional velocity components over the whole simulation period. The large-scale pattern of the MAGREF-MAGTRUTH misfit of the $\sigma-$depth$-$integrated velocities are in agreement with the MAGREF-MAGTRUTH misfit of the ocean-induced magnetic field (compare Figures 5 and 7). Naturally, the misfit of the $\sigma-$depth$-$integrated velocities shows more small-scale features that are not visible in the magnetic field misfit due to the upwardly continuation of the signal to satellite altitude. Additionally, it is visible that RMS differences of the zonal velocity close to the geomagnetic equator are weakened significantly in the RMS differences of the ocean-induced magnetic field, e.g., north east of Madagascar or in the equatorial region of the East Pacific Ocean. Since the motional induction signal is close to zero in proximity of the geomagnetic equator, this intrinsic 'observation blindness' provides an additional challenge to the Kalman filter.

A comparison of Figures 2 and 7 allows drawing relations between the major ocean currents, the RMS differences between MAGREF and MAGTRUTH, and the assimilation impact in the regions of the respective currents, respectively. In comparison with the assimilation impact of the ocean-induced magnetic field

(Figure 5), the $\sigma-$depth$-$integrated velocities show similar large-scale improvements with values over -40 S ms^{-1} ($\approx$ 30%) in the North Pacific Ocean. Especially in the region of the Kuroshio current, large improvements over -60 S ms^{-1} ($\approx$ 50%) are found. In the Antarctic Circumpolar Current, the largest improvements are found east of South Africa, with values over -50 S ms^{-1} ($\approx$ 30%) (Figure 7, bottom row). Peak values of the improvement reach over -100 S ms^{-1} in the North Pacific Ocean. In the equatorial region of the zonal currents, the transport is corrected by up to -20 S ms^{-1} ($\approx$ 25%), and in the region of the Gulf stream by up to -10 Sms^{-1} ($\approx$ 15%). Since the strongest ocean-induced magnetic field signals and respective variations occur in the region of the Antarctic Circumpolar Current (compare Figure 3), it was common to assume that improvements due to data assimilation are also mainly confined to regions in the southern hemisphere. Consequently, the shown large-scale improvements in the northern hemisphere, especially in the North Pacific Ocean, are both surprising and encouraging for the application of this technique.

In general, the deterioration pattern between the ocean-induced magnetic field and the $\sigma-$depth$-$integrated velocities also coincide (compare Figures 5 and 7). The largest deteriorations with values between 30 and 40 S ms^{-1} occur for both velocity components in the South Pacific Ocean between the Ross Sea and the southern tip of South America. Further false corrections by the Kalman filter are visible in the zonal velocity in the Northwest Indian Ocean close to the geomagnetic equator.

The most likely source of these false correction is a deficient prescription of the error covariance information in P_t for that particular region, which is solely based on the temporal covariances of MAGREF (see section 2.2.2). An accurate calculation of the error covariances is a challenge and the estimation of these is not unique [*Irrgang et al.*, 2016b]. However, the current configuration of the Kalman filter functions remarkably well in improving the ocean-induced magnetic field and the $\sigma-$depth$-$integrated velocities in most regions, given the blurry and noisy magnetic field observations. Further constraints on the error covariances, especially for the wind stress forcing, could resolve the major deteriorations found in the South Pacific Ocean and further reduce the differences between the ocean model and the known true ocean state.

Over simulation periods longer than 1 month, the impact of the Kalman filter on the ocean model state becomes negligible. The model uncertainty decreases during each assimilation step, which eventually leads to an underestimation of the model variance (not shown). Thereby, the confidence in the ocean model state and in the adjusted wind stress forcing rises continuously compared to the confidence in the observations. This reduces the Kalman filter increments in each assimilation step. Consequently, the MAGASSIM and MAG-TRUTH model trajectories gradually diverge due to the nonlinear ocean model and due to the nonstatic atmospheric forcing. This is a well-known behavior [e.g., *Furrer and Bengtsson*, 2007] and might be overcome in subsequent studies by applying additional covariance inflation techniques [e.g., *Anderson*, 2007] or sequential assimilation experiments over consecutive simulation periods that utilize specific error covariance matrices.

The biggest challenge in assimilating ocean-induced magnetic field satellite observations is the improvement of the separate ocean variables that determine the motional induction, i.e., ocean velocities, temperature, and salinity. The impact of the Kalman filter on each of these four variables is depicted in Figures 8 and 9.

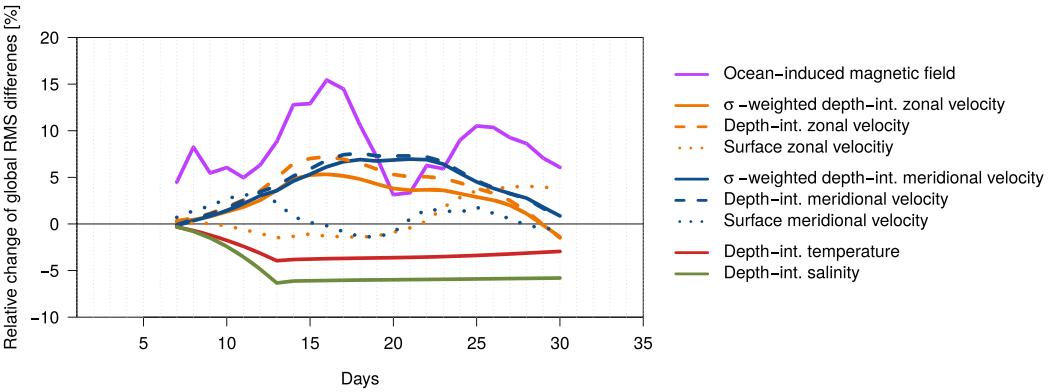

Figure 8. Relative changes of the global RMS differences. Positive values indicate improvements of the respective quantities, negative values indicate deteriorations.

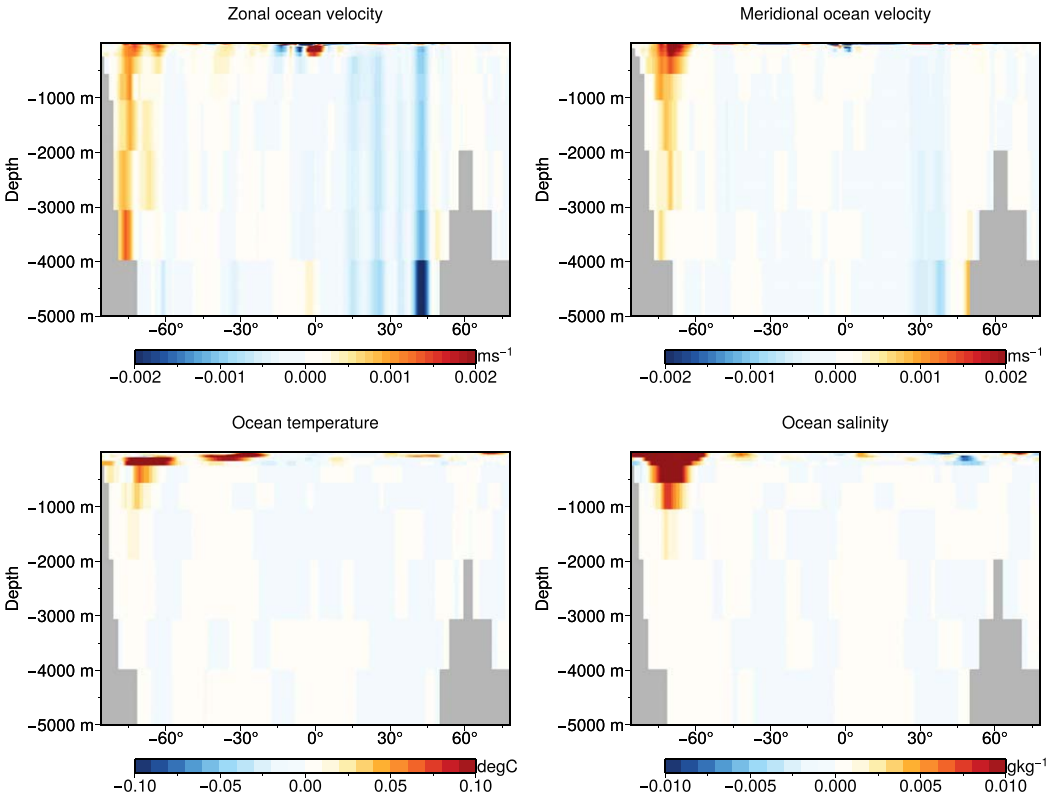

Figure 9. Zonally (west-east) averaged depth-profiles of the assimilation impact over the whole simulation period. Blue areas indicate improvements, red areas indicate deteriorations.

Figure 8 shows the relative change of the global RMS differences for each variable over the whole simulation period. In addition to the curves of the ocean-induced magnetic field and the $\sigma-$depth$-$integrated velocities presented before (see gray lines in Figures 4 and 6), the respective curves for depth-integrated velocities, surface velocities, temperature, and salinity are plotted. The changes in the RMS differences of ocean temperature and salinity reveal that the Kalman filter fails to improve these quantities (green and red lines in Figure 8) during all assimilation steps. Although the deterioration gradually decreases over time after day 13, the values mostly remain between -2 and -3% for the depth-integrated temperature and between -4 and -5% for the depth-integrated salinity. One explanation of this false shift is a possibly deficient estimation of the temperature and salinity error covariances for the simulated time period. The combined false shift in the two components is transferred to the sea water conductivity and, subsequently, to the $\sigma-$depth$-$integrated velocities. Thereby, the depth-integrated zonal and meridional velocities show a larger improvement than the respective conductivity-weighted quantities (see dashed blue and orange lines in Figure 8). The difference between the conductivity-weighted and nonweighted depth-integrated velocities amounts to up to 2% points (compare solid and dashed blue and orange lines in Figure 8). It was possible to weaken the false shift in the ocean temperature and salinity, by reducing the Kalman filter increments of the two variables in each assimilation step (not shown). However, it is important to demonstrate the challenge of improving the whole ocean state consistently. A second challenge becomes apparent, when the relative changes in RMS differences of depth-integrated ocean velocities and of surface velocities are compared (compare dashed and dotted blue and orange lines in Figure 8). In contrast to the water transport over the whole water column, surface currents are not improved consistently over the simulation period. The respective relative changes in the RMS differences of the surface velocities are generally smaller than changes in the depth-integrated quantities and fluctuate between -2 and 5%. Not surprisingly, this result shows that a consistent global correction of oceanic transports at individual layers of the ocean model is difficult due to the integral magnetic field observations. For this, additional constraints are necessary, which relate the observed ocean-induced magnetic field to its electromagnetic source at individual depths of the ocean.

In addition to showing the assimilation improvements in a depth-integrated sense, Figure 9 depicts the Kalman filter impact as zonally and temporally averaged cross sections of the global ocean for each oceanic quantity. This allows associating the Kalman filter impact (in depth-integrated sense as seen in Figure 7) with specific depths. The zonal and meridional ocean velocities show improvements over large regions of the cross sections that reach from the sea surface down to the ocean bottom (Figure 9, upper left and right). Most prominent regions are found in the northern hemisphere between 0° and 60°. Consequently, the previously described improvements of the $\sigma-$depth$-$integrated velocities in the North Pacific Ocean (Figure 7, bottom) result from a state shift toward the true state over the whole water column. In contrast, the improvements found in the equatorial region of the $\sigma-$depth$-$integrated zonal velocities mainly originate from a state correction in the upper 250 m (compare Figure 7 (lower left) and Figure 9 (upper left)). Likewise, the deterioration of the $\sigma-$depth$-$integrated zonal velocity in the northwest Indian Ocean also originates from a false correction in the upper 250 m. The most prominent false corrections in the ocean-induced magnetic field and in the $\sigma-$depth$-$integrated velocities in the South Pacific Ocean (Figures 5 and 7) dominantly originate from deteriorations in the zonal and meridional velocities over the whole water columns. These are additionally intensified by false corrections of the ocean salinity and temperature in the upper 1000 m south of $-60°$ (Figure 9, bottom).

A consistent correction of the wind stress forcing together with the ocean model state is found to be essential for the described results of the data assimilation. In a twin experiment without wind stress correction (otherwise identical to the twin experiment of this study), the Kalman filter failed to improve both the ocean model state and the ocean-induced magnetic field (not shown). Previously, *Saynisch et al.* [2014] also recognized the need to correct the wind stress forcing in order to improve trajectories of an ocean general circulation model. This repeatedly underlines the fragility of data assimilation in ocean models. The temporal mean correction of the wind stress forcing estimated by the Kalman filter and the respective assimilation impact are shown in Figure 10. Most values reside in the range of $\pm$ 0.1 Pa. The large-scale wind stress corrections are well in agreement with the uncertainty estimation of the ocean-induced magnetic field [see *Irrgang et al.*, 2016b] and, subsequently, with the assimilation impact of the ocean-induced magnetic field and of the $\sigma-$depth$-$integrated velocities (compare Figure 10 (top row) with Figures 5 and 7). This points out the close connection of the error covariances between the ocean state and the wind stress forcing. In the regions of highest wind stress adjustment, the vertical adjustment of the ocean velocities mostly extends over the whole water column (see Figure 9). In particular, Figure 10 (top row) shows a considerable adjustment of the wind stress forcing in the South Pacific Ocean, where the largest deteriorations in the ocean-induced magnetic field and in the $\sigma-$depth$-$integrated velocities are detected. Consequently, the false corrections by the Kalman filter are assumed to dominantly originate from a deficient estimation of the error covariances between the wind stress forcing and the ocean model state, and a false adjustment of the wind stresses in this region. This is further emphasized by the assimilation impact on the wind stress forcing (see Figure 10, bottom row). As it was shown for the $\sigma-$depth$-$integrated velocities in Figure 7, the blue areas represent improvements due to the Kalman filtering, whereas red areas indicate deteriorations. The major deteriorations, which are visible in the North and South Pacific Ocean, largely coincide with the major deteriorations in the $\sigma-$depth$-$integrated velocities (compare Figures 7 and 10 (bottom row)). These overestimated adjustments are attributed to the functionality of the Kalman filter, as corrections of the wind stress forcing are based on static error covariance matrices instead of dynamic ensemble-based correction estimates. However, in most regions, large-scale improvement of RMS differences of both zonal and meridional wind stresses are visible. As stated before, these adjustments are found to be essential for a successful assimilation.

The assimilation of synthetic ocean-induced magnetic field satellite observations into an ocean general circulation model shows very promising results. Despite the low amount of detail in the blurry observations, the Kalman filter succeeded to improve the ocean model results in all erroneous regions. Additionally, the observations positively constrained ocean velocities from the sea surface down to the deep ocean. This study highlights that actual satellite observations of the general circulation induced magnetic field could be utilized to constrain large-scale oceanic transports. Subsequent studies may demonstrate the sensitivity of the assimilation toward the data quality (e.g., nonuniform noise, spatial and temporal gaps, residuals from other electromagnetic sources, etc.). In turn, it might be possible to provide minimum requirements of the quality of actual magnetic field observations for a successful data assimilation. Our results emphasize the

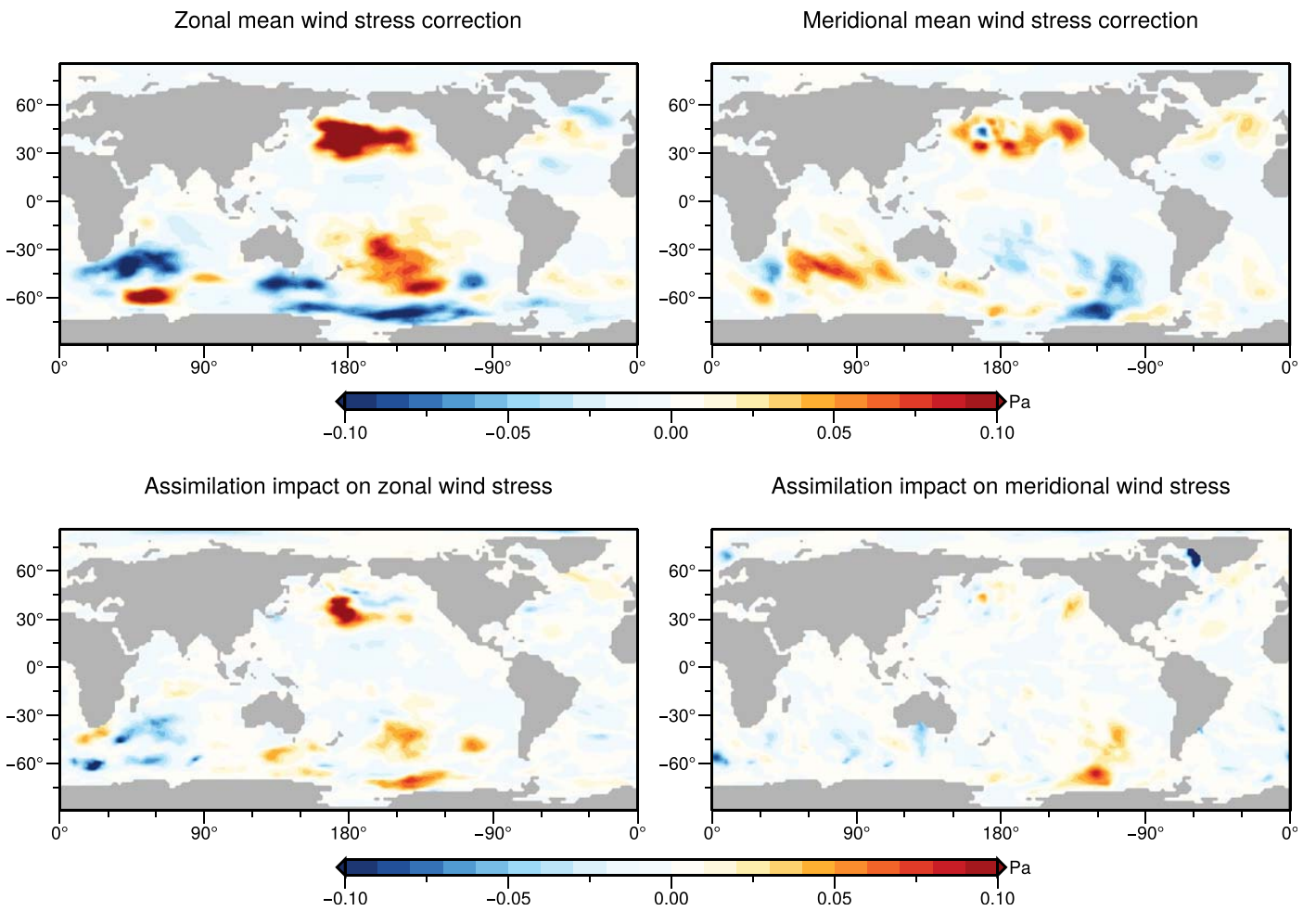

Figure 10. (top) Temporal mean wind stress forcing corrections due to the Kalman filtering. The maps show ensemble mean values. (bottom) Changes in the RMS differences of the wind stress forcing due to Kalman filtering. Blue areas indicate improvements, red areas indicate deteriorations.

need for a careful treatment of model uncertainties and error covariances. Aside from the quality of the observational data, the knowledge about model and forcing uncertainties is crucial for a successful data assimilation.

4. Summary and Conclusion

The general ocean circulation generates characteristic magnetic signals that in principle can be detected by low earth orbit satellites like the Swarm mission. Since these magnetic signals are mainly proportional to the conductivity-weighted and depth-integrated ocean velocities, the satellite observations may serve as indirect observations of global oceanic water and heat transports. In this study, we investigate the potential to correct an ocean general circulation model by assimilating artificial satellite observations of the ocean-induced magnetic field for the first time. In a model-based twin experiment over the time period of one month, the impact of the data assimilation on the individual components of the oceanic electromagnetic induction source is estimated, i.e., ocean velocities, ocean temperature, and ocean salinity.

Due to the difficult separability of the general circulation induced magnetic field from other electromagnetic sources, these signals have so far not yet been detected in satellite observations. Instead, we assume that a data product exists that contains idealized daily global observation fields of the ocean-induced magnetic field at satellite altitude. The synthetic satellite observations are calculated with a combination of an ocean general circulation model and an electromagnetic induction model. Observational errors are modeled by adding uncorrelated Gaussian white noise to the calculated magnetic signals. These synthetic

observations are sequentially assimilated into the ocean model. The data assimilation is performed by a localized version of an ensemble-based error subspace Kalman filter. This Kalman filter is integrated into the ocean model and corrects zonal and meridional ocean velocities, ocean temperature, and ocean salinity, and wind stresses from the atmospheric forcing of the ocean model.

Compared to a reference simulation without data assimilation, the simulation corrected by the Kalman filter performs better in recovering the synthetic observations throughout the whole simulation period. The global RMS error of the ocean-induced magnetic field is reduced by up to 17%. Locally, the RMS reduction amounts up to 42% in the North Pacific Ocean and up to 54% in the region east of South Africa. All spatial regions with large RMS errors in the reference simulation, e.g., in the North Pacific Ocean, east of Australia, and east of South Africa, are improved in the simulation with data assimilation. In particular, the results demonstrate the feasibility to correct an ocean model in areas with comparable weak induced magnetic field observations, e.g., in the North Pacific Ocean and in equatorial regions. False corrections are introduced in the South Pacific Ocean that originate from false adjustments in the conductivity-weighted and depth-integrated ocean velocities. The main source of false corrections is presumably due to the combined effect of large wind stress forcing adjustments and a deficient estimation of ocean model and wind stress error covariances. In an identical twin experiment without correction of the wind stress from the atmospheric forcing of the ocean model, it was not possible to recover the synthetic observations.

The conductivity-weighted and depth-integrated velocities are improved throughout the simulation period (in the global RMS sense) with values up to 5% for the zonal component and up to 7% for the meridional component. Locally, the improvements of water transports in individual ocean currents reach higher values, e.g., over 30% in the Antarctic Circumpolar Current, over 50% in the Kuroshio current, over 15% in the Gulf Stream, and over 25% in the equatorial region of the Pacific Ocean. The improved regions coincide with the improved regions of the ocean-induced magnetic field. Global RMS differences of the individual components reveal that the Kalman filter fails to improve ocean temperature and salinity. However, vertical cross sections of the individual ocean variables reveal that respective improvements in the ocean velocities mostly extend from the sea surface down to the deep ocean, whereas deteriorations in the ocean temperature and salinity mostly reside in the upper 1000 m of the Southern Ocean. Since all major deteriorations in the ocean model state are introduced in regions with major corrections of the wind stresses, a more dynamical estimation of the error covariances between the ocean state and the atmospheric forcing might diminish these false corrections.

The results of this study show that satellite observations of the ocean-induced magnetic field could provide useful constraints on depth-integrated ocean variables, e.g., oceanic water and heat transports. Although even the idealized synthetic satellite observations only provide a small amount of detail, the Kalman filter succeeded to better recover both the ocean-induced magnetic field and the underlying ocean state in most regions. Consequently, these results support the ongoing effort to separate ocean circulation induced magnetic signals in satellite observations. However, actual satellite observations will naturally differ from the idealized data generated for this study. Among others, these differences result from the simplified physics in the electromagnetic induction model, the considered time period, temporal and spatial gaps in the observations, and remaining residuals from other electromagnetic induction sources. The same holds for the spatiotemporal distribution of observational uncertainty, which is assumed uniform in this study. Actual satellite observations will contain spatially and temporally nonuniform errors. In addition, these errors can contain error correlation due to untreated magnetic signal residuals from other electromagnetic sources (e.g., from the magnetosphere or the Earth's crust). Consequently, potential observational error correlations also need to be accounted for in real-world data assimilation experiments. Future studies might provide minimum constraints on the data quality necessary to gain useful constraints on the underlying general ocean circulation. From the ocean modeling perspective, the results of this study emphasize the crucial need for realistic and dynamic error covariance matrices. In addition to the quality of the data, knowledge about model and forcing uncertainties is essential for a successful data assimilation.

Acknowledgments
We thank the Editor Robert Pincus, Associate Editor Dick Dee, Alexey Kuvshinov, and the anonymous reviewers for their insightful feedback and remarks, which helped to improve this manuscript considerably. This work has been funded by the Helmholtz graduate research school GeoSim and by the Helmholtz Centre Potsdam GFZ German Research Centre for Geosciences. The ocean model used for this study has been forced by the ERA-Interim data from the European Centre for Medium-Range Weather Forecasts. All numerical simulations were performed on the Mistral super computer from the German High Performance Computing Centre for Climate- and Earth System Research (DKRZ). We thank Lars Nerger for continuously developing and providing his Parallel Data Assimilation Framework. Researchers interested in using data from the OMCT may contact Maik Thomas (maik.thomas@gfz-potsdam.de). The compiled data of this study can be accessed through ftp://ftp.gfz-potsdam.de/home/ig/irrgang/JAMES/.

References

Anderson, J. L. (2007), An adaptive covariance inflation error correction algorithm for ensemble filters, *Tellus, Ser. A*, *59*(2), 210–224, doi: 10.1111/j.1600-0870.2006.00216.x.

Chaudhuri, A. H., R. M. Ponte, G. Forget, and P. Heimbach (2013), A comparison of atmospheric reanalysis surface products over the ocean and implications for uncertainties in air–sea boundary forcing, *J. Clim.*, *26*(1), 153–170, doi:10.1175/JCLI-D-12-00090.1.

Chave, A. D. (1983), On the theory of electromagnetic induction in the Earth by ocean currents, *J. Geophys. Res.*, *88*(B4), 3531–3542, doi:10.1029/JB088iB04p03531.
Chave, A. D., and D. S. Luther (1990), Low-frequency, motionally induced electromagnetic fields in the ocean: 1. Theory, *J. Geophys. Res.*, *95*(C5), 7185–7200.
Cox, C. S. (1981), On the electrical conductivity of the oceanic lithosphere, *Phys. Earth Planet. Inter.*, *25*(3), 196–201, doi:10.1016/0031-9201(81)90061-3.
Dee, D. P., et al. (2011), The ERA-Interim reanalysis: Configuration and performance of the data assimilation system, *Q. J. R. Meteorol. Soc.*, *137*(656), 553–597, doi:10.1002/qj.828.
Dobslaw, H., and M. Thomas (2007), Simulation and observation of global ocean mass anomalies, *J. Geophys. Res.*, *112*, C05040, doi:10.1029/2006JC004035.
Dobslaw, H., F. Flechtner, I. Bergmann-Wolf, C. Dahle, R. Dill, S. Esselborn, I. Sasgen, and M. Thomas (2013), Simulating high-frequency atmosphere-ocean mass variability for dealiasing of satellite gravity observations: AOD1B RL05, *J. Geophys. Res.*, *118*, 3704–3711, doi:10.1002/jgrc.20271.
Dostal, J., Z. Martinec, and M. Thomas (2012), The modelling of the toroidal magnetic field induced by tidal ocean circulation, *Geophys. J. Int.*, *189*(2), 782–798, doi:10.1111/j.1365-246X.2012.05407.x.
Evensen, G. (1994), Inverse methods and data assimilation in nonlinear ocean models, *Physica D*, *77*(1–3), 108–129, doi:10.1016/0167-2789(94)90130-9.
Evensen, G. (2003), The ensemble Kalman filter: Theoretical formulation and practical implementation, *Ocean Dyn.*, *53*(4), 343–367, doi:10.1007/s10236-003-0036-9.
Everett, M. E., S. Constable, and C. G. Constable (2003), Effects of near-surface conductance on global satellite induction responses, *Geophys. J. Int.*, *153*(1), 277–286, doi:10.1046/j.1365-246X. 2003.01906.x.
Flosadóttir, A. H., J. C. Larsen, and J. T. Smith (1997), Motional induction in North Atlantic circulation models, *J. Geophys. Res.*, *102*(C5), 10,353–10,372, doi:10.1029/96JC03603.
Friis-Christensen, E., H. Lühr, and G. Hulot (2006), Swarm: A constellation to study the Earth's magnetic field, *Earth Planets Space*, *58*(4), 351–358, doi:10.1186/BF03351933.
Furrer, R., and T. Bengtsson (2007), Estimation of high-dimensional prior and posterior covariance matrices in Kalman filter variants, *J. Multivariate Anal.*, *98*(2), 227–255, doi:10.1016/j.jmva.2006.08.003.
Grayver, A. V., N. R. Schnepf, A. V. Kuvshinov, T. J. Sabaka, C. Manoj, and N. Olsen (2016), Satellite tidal magnetic signals constrain oceanic lithosphere-asthenosphere boundary, *Sci. Adv.*, *2*(9), e1600798, doi:10.1126/sciadv.1600798.
Greatbatch, R. J. (1994), A note on the representation of steric sea level in models that conserve volume rather than mass, *J. Geophys. Res.*, *99*(C6), 12,767–12,771, doi:10.1029/94JC00847.
Irrgang, C., J. Saynisch, and M. Thomas (2016a), Impact of variable seawater conductivity on motional induction simulated with an ocean general circulation model, *Ocean Sci.*, *12*, 129–136, doi:10.5194/os-12-129-2016.
Irrgang, C., J. Saynisch, and M. Thomas (2016b), Ensemble simulations of the magnetic field induced by global ocean circulation: Estimating the uncertainty, *J. Geophys. Res. Oceans*, *121*, 1866–1880, doi:10.1002/2016JC011633.
Kalman, R. E. (1960), A new approach to linear filtering and prediction problems, *Trans. ASME J. Basic Eng.*, *82*(1), 35–45, doi:10.1115/1.3662552.
Kuvshinov, A. (2008), 3-D global induction in the oceans and solid earth: Recent progress in modeling magnetic and electric fields from sources of magnetospheric, ionospheric and oceanic origin, *Surv. Geophys.*, *29*(2), 139–186, doi:10.1007/s10712-008-9045-z.
Larsen, J. C. (1968), Electric and magnetic fields induced by deep sea tides, *Geophys. J. R. Astron. Soc.*, *16*, 47–70, doi:10.1111/j.1365-246X.1968.tb07135.x.
Laske, G., and G. Masters (1997), A global digital map of sediment thickness, *Eos Trans. AGU*, *78*(46), F483.
Lilley, F. E. M., J. H. Filloux, P. J. Mulhearn, and I. J. Ferguson (1993), Magnetic signals from an ocean eddy, *J. Geomag. Geoelectr.*, *45*(5), 403–422, doi:10.5636/jgg.45.403.
Manoj, C., A. Kuvshinov, S. Maus, and H. Lühr (2006), Ocean circulation generated magnetic signals, *Earth Planets Space*, *58*(4), 429–437, doi:10.1186/BF03351939.
Maus, S., and A. Kuvshinov (2004), Ocean tidal signals in observatory and satellite magnetic measurements, *Geophys. Res. Lett.*, *31*, L15313, doi:10.1029/2004GL020090.
Maus, S., C. Manoj, J. Rauberg, I. Michaelis, and H. Lühr (2010), NOAA/NGDC candidate models for the 11th generation International Geomagnetic Reference Field and the concurrent release of the 6th generation Pomme magnetic model, *Earth Planets Space*, *62*(10), 729–735, doi:10.5047/eps.2010.07.006.
Nerger, L., W. Hiller, and J. Schröter (2005a), A comparison of error subspace Kalman filters, *Tellus, Ser. A*, *57*(5), 715–735, doi:10.1111/j.1600-0870.2005.00141.x.
Nerger, L., W. Hiller, and J. Schröter (2005b), PDAF—The parallel data assimilation framework: Experiences with Kalman filtering, in *Proceedings of the 11. ECMWF Workshop on Use of High Performance Computing in Meteorology*, pp. 63–83, World Sci., Singapore.
Nerger, L., T. Janjić, J. Schröter, and W. Hiller (2012a), A unification of ensemble square root Kalman filters, *Mon. Weather Rev.*, *140*(7), 2335–2345, doi:10.1175/MWR-D-11-00102.1.
Nerger, L., T. Janjić, J. Schröter, and W. Hiller (2012b), A regulated localization scheme for ensemble-based Kalman filters, *Q. J. R. Meteorol. Soc.*, *138*(664), 802–812, doi:10.1002/qj.945.
Olsen, N., R. Haagmans, T. J. Sabaka, A. Kuvshinov, S. Maus, M. E. Purucker, M. Rother, V. Lesur, and M. Mandea (2006), The Swarm End-to-End mission simulator study: A demonstration of separating the various contributions to Earth's magnetic field using synthetic data, *Earth Planets Space*, *58*(4), 359–370, doi:10.1186/BF03351934.
Olsen, N., T. J. Sabaka, and L. R. Gaya-Pique (2007), Study of an improved comprehensive magnetic field inversion analysis for Swarm, final report, Danisch Natl. Sci. Cent., kgs, Lyngby.
Parkinson, W. D., and V. R. S. Hutton (1989), *The Electrical Conductivity of the Earth*, vol. *3*, pp. 261–232, Academic, San Diego, Calif.
Pham, D. T. (2001), Stochastic methods for sequential data assimilation in strongly nonlinear systems, *Mon. Weather Rev.*, *129*, 1194–1207, doi:10.1175/1520-0493(2001)129 < 1194:SMFSDA>2.0.CO;2.
Pham, D. T., J. Verron, and M. Christine Roubaud (1998a), A singular evolutive extended Kalman filter for data assimilation in oceanography, *J. Mar. Syst.*, *16*(3–4), 323–340, doi:10.1016/S0924-7963(97)00109-7.
Pham, D. T., J. Verron, and L. Gourdeau (1998b), Singular evolutive Kalman filters for data assimilation in oceanography, *C. R. Acad. Sci., Ser. II*, *326*(4), 255–160.
Sabaka, T. J., R. H. Tyler, and N. Olsen (2016), Extracting ocean-generated tidal magnetic signals from Swarm data through satellite gradiometry, *Geophys. Res. Lett.*, *43*, 3237–3245, doi:10.1002/2016GL068180.

Sanford, T. B. (1971), Motionally induced electric and magnetic fields in the sea, *J. Geophys. Res.*, *76*(15), 3476–3492, doi:10.1029/JC076i015p03476.

Saynisch, J., and M. Thomas (2012), Ensemble Kalman filtering of Earth rotation observations with a global ocean model, *J. Geodyn.*, *62*, 24–29, doi:10.1016/j.jog.2011.10.003.

Saynisch, J., I. Bergmann-Wolf, and M. Thomas (2014), Assimilation of GRACE-derived oceanic mass distributions with a global ocean circulation model, *J. Geod.*, *89*(2), 121–139, doi:10.1007/s00190-014-0766-0.

Saynisch, J., M. Semmling, J. Wickert, and M. Thomas (2015), Potential of space-borne GNSS reflectometry to constrain simulations of the ocean circulation, *Ocean Dyn.*, *65*(11), 1441–1460, doi:10.1007/s10236-015-0886-y.

Saynisch, J., J. Petereit, C. Irrgang, A. Kuvshinov, and M. Thomas (2016), Impact of climate variability on the tidal oceanic magnetic signal—A model-based sensitivity study, *J. Geophys. Res. Oceans*, *121*, 5931–5941, doi:10.1002/2016JC012027.

Schnepf, N. R., A. Kuvshinov, and T. Sabaka (2015), Can we probe the conductivity of the lithosphere and upper mantle using satellite tidal magnetic signals?, *Geophys. Res. Lett.*, *42*, 3233–3239, doi:10.1002/2015GL063540.

Stephenson, D., and K. Bryan (1992), Large-scale electric and magnetic fields generated by the oceans, *J. Geophys. Res.*, *97*(C10), 15,467–15,480, doi:10.1029/92JC01400.

Szuts, Z. B. (2010), Relationship between ocean velocity and motionally induced electrical signals: 2. In the presence of sloping topography, *J. Geophys. Res.*, *115*, C06004, doi:10.1029/2009JC006054.

Thomas, M., J. Sündermann, and E. Maier-Reimer (2001), Consideration of ocean tides in an OGCM and impacts on subseasonal to decadal polar motion excitation, *Geophys. Res. Lett.*, *28*(12), 2457–2460, doi:10.1029/2000GL012234.

Tyler, R. H., L. A. Mysak, and J. M. Oberhuber (1997), Electromagnetic fields generated by a three-dimensional global ocean circulation, *J. Geophys. Res.*, *102*(C3), 5531–5551, doi:10.1029/96JC03545.

Tyler, R. H., S. Maus, and H. Lühr (2003), Satellite observations of magnetic fields due to ocean tidal flow, *Science*, *299*(5604), 239–241, doi:10.1126/science.1078074.

Vennerstrom, S., E. Friis-Christensen, H. Lühr, T. Moretto, N. Olsen, C. Manoj, P. Ritter, L. Rastätter, A. Kuvshinov, and S. Maus (2005), The impact of combined magnetic and electric field analysis and of ocean circulation effects on Swarm Mission performance, technical report, Danish Natl. Space Cent., Kgs. Lyngby, Denmark.

Vivier, F., E. Meier-Reimer, and R. H. Tyler (2004), Simulations of magnetic fields generated by the Antarctic Circumpolar Current at satellite altitude: Can geomagnetic measurements be used to monitor the flow?, *Geophys. Res. Lett.*, *31*, L10306, doi:10.1029/2004GL019804.